Raman scattering study of background electron density in InN: a hydrodynamical approach to the LO-phonon–plasmon coupled modes

2009 J. Phys.: Condens. Matter 21 415801

(http://iopscience.iop.org/0953-8984/21/41/415801)

J. Phys.: Condens. Matter **21** (2009) 415801 (6pp) doi:10.1088/0953-8984/21/41/415801

Raman scattering study of background electron density in InN: a hydrodynamical approach to the LO-phonon–plasmon coupled modes

R Cuscó[1], E Alarcón-Lladó[1], J Ibáñez[1], T Yamaguchi[2], Y Nanishi[2] and L Artús[1]

[1] Institut Jaume Almera (CSIC), Lluís Solé i Sabarís s.n., E-08028 Barcelona, Spain
[2] Faculty of Science and Engineering, Ritsumeikan University, 1-1-1 Noji-Higashi, Kusatsu, Shiga 525-8577, Japan

Received 30 July 2009, in final form 1 September 2009
Published 23 September 2009
Online at stacks.iop.org/JPhysCM/21/415801

Abstract

We use a hydrodynamical approach to analyse the long-wavelength LO-phonon–plasmon coupled modes observed in a set of high-quality MBE-grown InN epilayers with electron densities varying over one order of magnitude, from $\sim 2 \times 10^{18}$ to $\sim 2 \times 10^{19}$ cm^{-3}. The samples were characterized by scanning electron microscopy, x-ray diffraction and Hall measurements. The correlation observed between the E_2^{high} mode frequency, and hence residual strain, and the electron density measured in the layers indicates that the differences in background electron density may be associated with threading dislocations. Owing to the low Raman signal, only the L^- branch of the coupled modes can be unambiguously observed. The frequency of the L^- Raman peak is, however, sensitive enough to the free electron density to allow its determination from lineshape fits to the spectra. These were carried out using an extended hydrodynamical model. Given the small bandgap energy and large conduction band nonparabolicity of InN, suitable expressions for the optical effective mass and mean square velocity that enter the hydrodynamical model were derived. Electron density values extracted from L^- lineshape fits agree reasonably well with Hall determinations.

1. Introduction

InN is attracting a great deal of attention because of its remarkable material properties: narrow bandgap, small effective mass, high electron mobility and high drift velocity. InN is also unique among III–V semiconductors in that it exhibits an extreme electron accumulation at the surface [1]. A range of new application fields that can exploit InN's unique properties has been proposed. These encompass ultrafast electronics, chemical sensors, spintronic and hybrid semiconductor/superconductor devices [2].

Although in recent years the quality of InN films has been improved remarkably, owing to the large lattice mismatch with the substrate InN films grown on sapphire still contain a high density of dislocations and a substantial background electron density N_e. Raman scattering is a nondestructive technique well suited to characterize the crystal quality and strain state of such semiconductor layers. In addition, the study of the LO-phonon–plasmon coupled modes (LOPCM) by Raman scattering allows N_e to be determined in a contactless way. This is particularly important in the case of InN, since the presence of the accumulation layer complicates the analysis of the Hall effect measurements to obtain the free electron density in the 'bulk' of the layer. Raman scattering by LOPCMs can provide an alternative optical means to probe directly the free electron density in InN layers. Although Raman lineshape calculations based on the Lindhard–Mermin model have proven to yield accurate results, from a practical point of view it is desirable to have a simpler framework to extract the electron density from lineshape fits to the Raman spectra. The hydrodynamical model [3], with different degrees of sophistication [4], has been successfully applied to other III–V semiconductors to evaluate the free carrier density from Raman spectra.

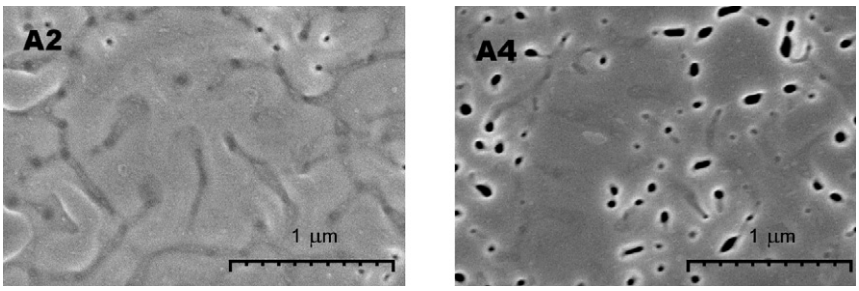

Figure 1. SEM images of the surface of N-polar InN layers A2 and A4 grown on nitrided sapphire substrates.

In this work we present a hydrodynamical approach to LOPCM lineshape modelling in InN. In order to properly take into account the high conduction band nonparabolicity of InN, a simplified two-band Kane's model is employed and closed expressions for the optical effective mass and mean square velocity are derived. This approach differs from previous treatments of nonparabolicity which used perturbative expansions of the relevant quantities in powers of $\alpha k_B T/E_G$, where α is the nonparabolicity coefficient, k_B is the Boltzmann constant and E_G is the bandgap energy [4, 5]. In the case of InN, its low bandgap energy renders such perturbative expansions unreliable for high carrier concentrations. The analysis of the LOPCMs by means of the extended hydrodynamical model (EHD) described in the present work, although much simpler than the full Lindhard–Mermin model, yields a determination of N_e that is not far from the results of the Lindhard–Mermin model and is consistent with the Hall data.

2. Experimental details

Six nominally undoped InN epilayers were grown at 450–500 °C by plasma-assisted molecular beam epitaxy (MBE). The samples were grown in two different MBE systems and are labelled accordingly (A1 to A4; B1 and B2). All of the samples were deposited on nitrided (0001) sapphire substrates except sample A1, which was grown on a GaN/sapphire template. All samples display n-type conductivity, as characterized by standard Hall measurements. The samples were also characterized by scanning electron microscopy (SEM) and x-ray diffraction (XRD). The sample characteristics are summarized in table 1. Raman scattering experiments were carried out at 80 K in a $z(x,\cdot)\bar{z}$ backscattering configuration, where z is parallel to the c axis. The Raman spectra were excited with the 514.5 nm line of an Ar^+ laser and recorded using a Jobin Yvon T64000 spectrometer equipped with a CCD detector cooled with liquid nitrogen. We estimate a Raman probing depth of $\approx$ 36 nm for the excitation used [6].

Figure 1 shows SEM images of the surface of samples A2 and A4. Some degree of surface roughness can be observed, with groove-like structures and pits scattered over the surface. The pits are more prominent and their density is higher for sample A4, which corresponds to a higher N_e (see table 1). Over a typical area probed by Raman scattering experiments (spot diameter $\sim$250 μm), a homogeneous distribution of surface roughness is observed and therefore the Raman measurements yield a representative average of the InN layer. Some inhomogeneous broadening of the Raman peaks can, however, be expected.

Table 1. Characteristics of the n-InN epilayers studied in this work: film thickness d, x-ray diffraction peak full width at half-maximum (FWHM), electron density N_e^{Hall} and mobility μ_{Hall} as determined from Hall measurements, and electron density N_e^{Raman} derived from L^- lineshape fits to the Raman spectra as explained in the text.

Sample series	A1	A2	A3	A4	B1	B2
d (nm)	550	1000	750	250	400	400
(0002) FWHM (arcmin)	9.6	2.4	2.5	2.1	0.8	1.0
$(10\bar{1}2)$ FWHM (arcmin)	38.4	33.3	36.3	45.0	47.9	39.3
N_e^{Hall} (10^{18} cm^{-3})	2.3	4.3	5.8	6.9	6.5	16
μ_{Hall} (cm^2 V^{-1} s^{-1})	1440	1090	930	900	954	684
N_e^{Raman} (10^{18} cm^{-3})	—	4.0	5.0	5.3	6.3	19

X-ray rocking curves (XRC) for the $(10\bar{1}2)$ and the (0002) planes were measured to evaluate the mosaicity of the layers, including the twist and tilt components. As can be seen in table 1, all the layers grown on sapphire show a consistently small and similar tilt component ((0002) FWHM), but the twist component ($(10\bar{1}2)$ FWHM) increases as the layer thickness decreases (samples A2 to A4).

3. Results and discussion

In wurtzite-type InN the E_2 and A_1(LO) modes are symmetry allowed in backscattering from a (0001) face. The nonpolar E_2 mode is very sensitive to the presence of biaxial strain in the layers. On the other hand, the polar A_1(LO) mode is polarized along z and its associated macroscopic electric field interacts with the background electron density. This may give rise to complex screening phenomena and LO-phonon–plasmon coupled modes (LOPCM). Raman scattering by these modes has been discussed previously in terms of wavevector nonconserving processes [7–10]. We have recently shown that Raman scattering by long-wavelength coupled modes takes place in InN [11]. Suitable lineshape fits to the L^- Raman peak can then be used to obtain the free electron density in InN layers.

Figure 2 displays a representative 80 K Raman spectrum of the InN layers (sample A3). The spectrum is dominated by the dipole-allowed E_2^{high} mode at $\approx$495 cm^{-1}. A weaker peak is observed at $\approx$593 cm^{-1} which is assigned to the A_1(LO) mode.

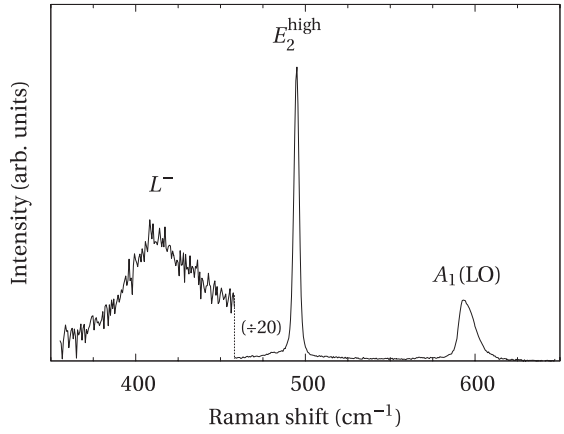

Figure 2. Representative Raman spectrum of the InN layers (sample A3) recorded at 80 K in backscattering configuration from a (0001) face.

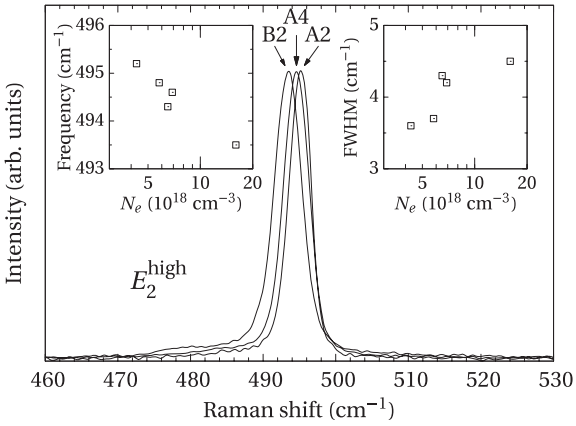

Figure 3. Raman spectra of the E_2^{high} mode for samples A2, A4 and B2. Insets: (top left) correlation between the frequency shift of the E_2^{high} mode and the background electron density in the samples; (top right) correlation between the full width at half-maximum of the E_2^{high} Raman peak and the background electron density.

This peak displays a visible shoulder on its high-frequency side that can be ascribed to the E_1(LO) mode. Although the E_1(LO) mode is symmetry forbidden in this configuration, it appears in the spectra due to the breakdown of selection rules induced by disorder and surface roughness. A much weaker and broader peak can be detected at ≈410 cm^{-1}. This peak is assigned to the L^- branch of the LOPCMs [11] and, as we shall see below, its frequency depends strongly on N_e. We have not been able to detect the L^+ branch of the LOPCMs in the InN spectra. Several factors may contribute to this. First, the overall Raman signal from LOPCMs in InN is very weak and a signal background associated with surface roughness is present in all the spectra. Second, according to the LOPCM model that we describe below, the intensity of the L^+ peak for the electron density range studied is lower than that of the L^- peak. Third, the L^+ has a plasmon-like character and its frequency is therefore much more sensitive to charge density variations. Fluctuations in the background electron density across the region probed by the laser spot may give rise to a smearing of the L^+ peak, making it undetectable in the noisy background.

The E_2^{high} mode is known to be sensitive to biaxial strain [12] whereas being a nonpolar mode, it is not affected by the presence of free charge. This makes it a good probe for biaxial strain in the layers. A correlation between the E_2^{high} frequency and N_e is found for the InN layers studied. In figure 3 we display the E_2^{high} peak for samples A2, A4 and B2. The E_2^{high} clearly broadens and shifts to lower frequencies as N_e increases. In the insets, the E_2^{high} frequency versus N_e and the E_2^{high} full width at half-maximum (FWHM) versus N_e are plotted for the whole set of samples. The broadening of the E_2^{high} mode for the layers with higher N_e reflects a lower crystalline quality (i.e. higher density of defects and impurities) in the volume probed by the laser. This suggests that the differences in N_e for the layers studied could be partly accounted for by the different level of incorporation of unintentional donor impurities [13, 14]. On the other hand, the downward frequency shift of the E_2^{high} mode indicates a relaxation of the residual compressive strain present in the InN layers [12]. Biaxial strain in the InN layers arising from lattice and thermal mismatch is relaxed by forming threading dislocations. The correlation observed between the E_2^{high} frequency and N_e therefore indicates that donor-type nitrogen vacancies associated with threading dislocations also play a role in determining the background electron density in InN layers [15].

The L^- coupled mode peak exhibits a large frequency shift (∼40 cm^{-1}) over the N_e range of the layers studied. A complete analysis of the LOPCM lineshapes was performed in [11] using the Lindhard–Mermin model, which yielded electron density values for the InN layers consistent with Hall determinations. Thus, Raman scattering emerges as an alternative tool to probe the bulk carrier concentration in InN layers. However, the full Lindhard–Mermin analysis is rather involved. For sample characterization purposes, a simpler and more direct approach to extract carrier density values from the Raman spectra is often desirable.

Since the typical electronic damping parameter in semiconductor plasmas is much larger than the phonon damping, we shall consider for simplicity the Raman scattering cross section in the zero phonon damping limit [16]

$$\mathcal{L}(\omega) \propto \left(\frac{\omega_{TO}^2(1+C)-\omega^2}{\omega_{TO}^2-\omega^2}\right)^2 \mathcal{IM}\left\{-\frac{1}{\varepsilon(\omega,q)}\right\}, \qquad (1)$$

where ω_{TO} is the frequency of the transverse optical phonon, C is the Faust–Henry coefficient and $\varepsilon(\omega, q)$ is the total dielectric function, which is given by

$$\varepsilon(\omega,q) = \varepsilon_\infty \frac{\omega_{LO}^2-\omega^2}{\omega_{TO}^2-\omega^2} + \varepsilon_e(q,\omega). \qquad (2)$$

Here ε_∞ is the high-frequency dielectric constant, ω_{LO} is the frequency of the longitudinal optical phonon, q is the excitation wavevector and $\varepsilon_e(q, \omega)$ is the dielectric function of the free

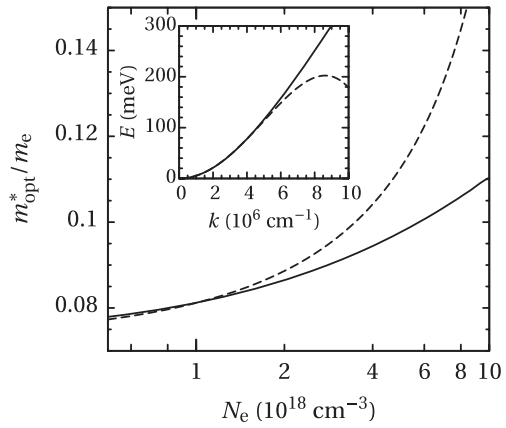

Figure 4. Optical effective mass as a function of electron density calculated from the **k** · **p** expression (solid line). The dashed line corresponds to the lowest-order expansion in the nonparabolicity coefficient α. Inset, comparison of the **k** · **p** conduction band dispersion (solid line) with its lowest-order expansion in α (dashed line).

electron gas. The latter may be evaluated using an EHD model [3, 4], which yields

$$\varepsilon_e(q,\omega) = -\varepsilon_\infty \frac{\omega_p^2}{\omega^2 - \langle v^2\rangle q^2 + i\omega\Gamma_e}, \tag{3}$$

where ω_p is the plasma frequency, Γ_e is a phenomenological electronic damping parameter and $\langle v^2\rangle$ is the mean square velocity of the electrons. Conduction band nonparabolicity and thermal distribution effects are taken into account in the EHD model by using the optical effective mass [17] in the evaluation of ω_p in equation (3). The mean square velocity is also evaluated using the Fermi distribution $f(E; E_F, T)$ corresponding to the assumed Fermi energy E_F and temperature T.

Given the low bandgap energy of InN, a substantial nonparabolicity of the conduction band is expected. Indeed, a strong dependence of the electron effective mass on the free electron energy as well as a concentration-dependent blueshift of the absorption edge has been reported in InN [18]. Nonparabolicity effects in semiconductors are commonly evaluated in terms of Fermi integrals by carrying out a perturbative expansion of the **k** · **p** conduction band dispersion in powers of $\alpha E(k)/E_G$ [4, 5]. However, in the case of InN ($\alpha \approx -0.8$, $E_G \approx 0.7$ eV) the correction rapidly increases with k and becomes dominant. This is illustrated in the inset of figure 4, where we can see that for $E_F \gtrsim 120$ meV the lowest order approximation to the conduction band dispersion substantially deviates from the full **k** · **p** energy dispersion and progressively flattens (dashed line). As can be seen in figure 4, this leads to an important overestimation of the optical effective mass and of the density of states at high carrier densities which affects the electron density determination from the LOPCM analysis. It should be underlined that the optical effective mass values obtained from the full **k** · **p** calculation (solid line in figure 4) are in good agreement with the experimental values reported in [18].

To avoid the inaccuracies introduced by the nonparabolicity expansion, band nonparabolicity was taken into account through an approximation of the two-band **k** · **p** Kane model [20] in the small effective mass limit which neglects spin–orbit interaction [2, 11]. The conduction band dispersion is then given by

$$E(k) = \frac{E_G}{2}\left[\sqrt{1 + \frac{4}{E_G}\frac{\hbar^2k^2}{2m^*}} - 1\right] \tag{4}$$

where m^* is the band-edge electron effective mass. By using equation (4), closed expressions for the electron density:

$$N_e = \frac{1}{2\pi^2}\left(\frac{2m^*}{\hbar^2}\right)^{\frac{3}{2}}\int_0^\infty \left(1+\frac{E}{E_G}\right)^{\frac{1}{2}}\left(1+\frac{2E}{E_G}\right) \times \frac{E^{\frac{1}{2}}}{1+\exp[(E-E_F)/k_BT]}\,dE, \tag{5}$$

the optical effective mass:

$$\frac{1}{m^*_{opt}} = \frac{\sqrt{2m^*}}{3\pi^2\hbar^3N_e}\int_0^\infty \left[3 - 4\frac{E(E_G+E)}{(E_G+2E)^2}\right]\left(1+\frac{E}{E_G}\right)^{\frac{1}{2}} \times \frac{E^{\frac{1}{2}}}{1+\exp[(E-E_F)/k_BT]}\,dE, \tag{6}$$

and the mean square velocity:

$$\langle v^2\rangle = \frac{1}{\pi^2N_em^*}\left(\frac{2m^*}{\hbar^2}\right)^{\frac{3}{2}}\int_0^\infty dE\left(1+\frac{E}{E_G}\right)^{\frac{3}{2}}\left(1+\frac{2E}{E_G}\right)^{-1} \times \frac{E^{\frac{3}{2}}}{1+\exp[(E-E_F)/k_BT]}\,dE \tag{7}$$

can be derived. Substituting equations (5)–(7) into equation (3) we obtain an expression for the electronic susceptibility with E_F and Γ_e as free parameters which we can use in equations (2) and (1) to obtain the Raman scattering cross section. The above integrals do not contain singularities and can be straightforwardly evaluated by using standard numerical integration methods.

The EHD lineshape model described above was fitted to the Raman spectra to extract the free electron density in the InN layers. The model parameter values used for InN are listed in table 2. The $z(x,\cdot)\bar{z}$ Raman spectra of the InN layers obtained at 80 K are displayed in figure 5 (lower panel). The L^- Raman signal was very weak and long integrations (∼1 h) were required to achieve an acceptable signal-to-noise ratio. For the high electron concentration present in sample B2, the L^- mode displays a strong phonon-like character and a relatively strong, narrow peak is observed in the Raman spectrum. The background electron density was significantly lower in the remaining layers. For these layers the L^- mode acquires a plasmon-like character and becomes weaker and broader as the electron density decreases. The higher sensitivity of the L^- frequency to N_e in this regime may contribute to smear out the L^- Raman peak due to inhomogeneities in the background electron distribution. As a result, the L^- Raman peak reduces its intensity, becoming barely visible in the spectrum of sample A2. For layer A1, the L^- Raman peak could not be unambiguously detected above

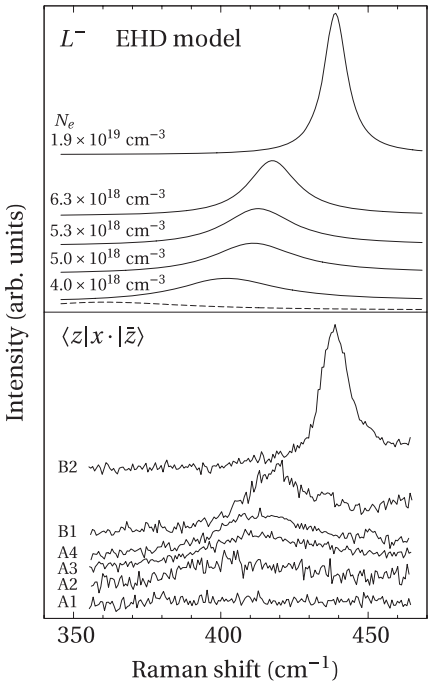

Figure 5. Lower panel: Raman spectra of the L^- coupled modes for all of the InN layers studied. Upper panel: L^- lineshapes calculated using the extended hydrodynamical model for the N_e and Γ_e values obtained from the model fit to the Raman spectra. The dashed line corresponds to $N_e = 2.3 \times 10^{18}$ cm^{-3}, as determined by Hall measurements for sample A1.

the noise level in our experiments. In the upper panel of figure 5 the calculated lineshape fits are plotted for the electron density values obtained from the fits to the corresponding Raman spectra. We can see that the EHD model nicely reproduces the experimental data. Both the frequency shift of the L^- mode and the L^- intensity variation with N_e are correctly predicted by the EHD model calculations. Using the EHD model, we can simulate the L^- Raman spectrum for sample A1 taking the electron density determined from Hall measurements. The calculated lineshape is plotted as a dashed line in figure 5. Since in sample A1 the background electron density is substantially reduced, the L^- mode shifts to lower frequencies and acquires a dominant plasmon-like character. As a consequence, its Raman intensity becomes very weak, which explains the absence of an unambiguous L^- feature in the Raman spectrum of sample A1.

The electron density values obtained from the lineshape fits agree well with those obtained from Hall determinations, and they are only between 4 and 6% lower than N_e values derived from the more involved Lindhard–Mermin model used in [11]. These small differences arise from the different approach to treat wavevector dispersion effects in the respective electronic susceptibility models. The hydrodynamical approach gives rise to a pole in the susceptibility at $\omega = \langle v^2 \rangle^{\frac{1}{2}} q$ (see equation (3)) which is absent in the Lindhard–Mermin treatment. Such a singularity distorts the susceptibility in the vicinity of the pole and slightly displaces the zeros of the dielectric function. However, in view of the uncertainty in the material parameters, the EHD model provides an adequate description of the coupled modes and an accurate determination of N_e with a less involved model.

Table 2. InN parameters used in the LOPCM lineshape model.

Symbol	Description	Value	Reference
ω_{LO}	A_1(LO) frequency	591.8 cm^{-1}	[a]
ω_{TO}	A_1 (TO) frequency	451.3 cm^{-1}	[a]
m^*	Electron effective mass	0.07 m_e	[b]
C	Faust–Henry coefficient	−2.0	[c]
E_G	Bandgap energy	650 meV	[d]
ε_∞	High-frequency dielectric constant	6.7	[d]

[a] 80 K strain-free values estimated from data in [12] and [19] and the temperature shift observed in our samples. For the lineshape fits, these values were corrected for strain according to the E_2^{high} frequency measured in each layer using data in [12].
[b] Reference [18].
[c] Reference [8].
[d] Reference [6].

4. Conclusions

Raman scattering can give information about the strain state and the background electron density of InN layers. Depending on growth conditions, InN morphology and background electron density may show significant variations. Raman measurements performed on a series of InN layers with different electron densities have revealed that the frequency of the E_2^{high} mode is correlated with the background electron density, which indicates that strain relaxation through threading dislocations favours the presence of donor-type defects such as nitrogen vacancies. Similarly, a correlation between the E_2^{high} FWHM and N_e has also been observed, which in turn suggests a higher rate of unintentional impurity incorporation in the InN layers with higher N_e.

Raman scattering can also provide an alternative tool to characterize the background electron density in the InN layers. The L^- coupled modes could be detected in all the layers but the one with the lowest electron density and they show a substantial frequency shift across the range of electron densities studied. The use of an EHD approach to LOPCM modelling simplifies the lineshape calculations while retaining the essential physical features of the LOCPM analysis, namely conduction band nonparabolicity, wavevector dispersion and thermal distribution effects. For the case of InN, the usual perturbative expansions in the nonparabolicity coefficient of the $\mathbf{k}\cdot\mathbf{p}$ expressions are not valid. Instead, closed expressions derived from Kane's secular equation were used in the EHD model.

The EHD accurately reproduces both the frequency and the intensity of the L^- Raman peak. Lineshape fits allowed us to extract the background electron density from the L^- Raman spectra of the InN layers. The N_e values thus obtained are within ∼6% of those derived from the more sophisticated Lindhard–Mermin model and agree well with the Hall measurement determinations. The EHD provides a convenient tool to analyse the L^- coupled mode spectra of

InN and to obtain a contactless determination of the electron density in InN layers.

Acknowledgments

This work has been supported by the Spanish Ministry of Science and Innovation under contract MAT 2007-63617 and by the FPI Programme.

References

[1] Lu H, Schaff W J, Eastman L F and Stutz C E 2003 *Appl. Phys. Lett.* **82** 1736
[2] Veal T D, Piper L F J, Schaff W J and McConville C F 2006 *J. Cryst. Growth* **288** 268
[3] Nowak U, Richter W and Sachs G 1981 *Phys. Status Solidi* b **108** 131
[4] Ibáñez J, Cuscó R and Artús L 2001 *Phys. Status Solidi* b **223** 715
[5] Blakemore J S 1982 *J. Appl. Phys.* **53** R123
[6] Kasic A, Valcheva E, Monemar B, Lu H and Schaff W J 2004 *Phys. Rev.* B **70** 115217
[7] Thakur J S, Haddad D, Naik V M, Naik R, Auner G W, Lu H and Schaff W J 2005 *Phys. Rev.* B **71** 115203
[8] Demangeot F, Pinquier C, Frandon J, Gaio M, Briot O, Maleyre B, Ruffenach S and Gil B 2005 *Phys. Rev.* B **71** 104305
[9] Pomeroy J W, Kuball M, Swartz C H, Myers T H, Lu H and Schaff W J 2007 *Phys. Rev.* B **75** 035205
[10] Kasic A, Schubert M, Saito Y, Nanishi Y and Wagner G 2002 *Phys. Rev.* B **65** 115206
[11] Cuscó R, Ibáñez J, Alarcón-Lladó E, Artús L, Yamaguchi T and Nanishi Y 2009 *Phys. Rev.* B **79** 155210
[12] Wang X, Che S B, Ishitani Y and Yoshikawa A 2006 *Appl. Phys. Lett.* **89** 171907
[13] Stampfl C, Van de Walle C G, Vogel D, Kruger P and Pollmann J 2000 *Phys. Rev.* B **61** R7846
[14] Look D C, Lu H, Schaff W J, Jasiniski J and Liliental-Weber Z 2002 *Appl. Phys. Lett.* **80** 258
[15] Piper L F J, Veal T D, McConville C F, Lu H and Schaff W J 2002 *Appl. Phys. Lett.* **88** 252109
[16] Irmer G, Toporov V V, Bairamov B H and Monecke J 1983 *Phys. Status Solidi* b **119** 595
[17] Cardona M 1961 *Phys. Rev.* **121** 752
[18] Wu J, Walukiewicz W, Shan W, Yu K M, Ager J W III, Haller E E, Lu H and Schaff W J 2002 *Phys. Rev.* B **66** 201403
[19] Davydov V Yu, Emtsev V V, Goncharuk I N, Smirnov A N, Petrikov V D, Mamutin V V, Vekshin V A, Ivanov S V, Smirnov M B and Inushima T 1999 *Appl. Phys. Lett.* **75** 3297
[20] Kane E O 1957 *J. Phys. Chem. Solids* **1** 249